Supplementary Information for

Magnetic signatures and origins of ferromagnetic minerals in Chang'e-6 lunar farside soils

Jinhua Li[1,2*], Lin Xing[1,2], Zheng Gong[3], Jiawei Liu[2,4], Yan Liu[1,2], Weiwei Wu[1,2], Kelei Zhu[1,2], Yuqin Wang[1,2], Xu Tang[1,2], Lixin Gu[1,2], Yi Chen[2,5], Qiuli Li[2,5], Zhaoyang Cao[1,2], Shuangchi Liu[2,5], Shuhui Cai[2,5], Yongxin Pan[2,4]

[1]Key Laboratory of Deep Petroleum Intelligent Exploration and Development, Institute of Geology and Geophysics, Chinese Academy of Sciences, Beijing 100029, China

[2]College of Earth and Planetary Sciences, University of Chinese Academy of Sciences, Beijing 100049, China

[3]State Key Laboratory for Critical Earth Material Cycling and Mineral Deposits, School of Earth Sciences and Engineering, Nanjing University, Nanjing 210023, China

[4]Key Laboratory of Earth and Planetary Physics, Institute of Geology and Geophysics, Institute of Geology and Geophysics, Chinese Academy of Sciences, Beijing 100029, China

[5]State Key Laboratory of Lithospheric and Environmental Coevolution, Institute of Geology and Geophysics, Chinese Academy of Sciences, Beijing 100029, China

*E-mail: lijinhua@mail.iggcas.ac.cn

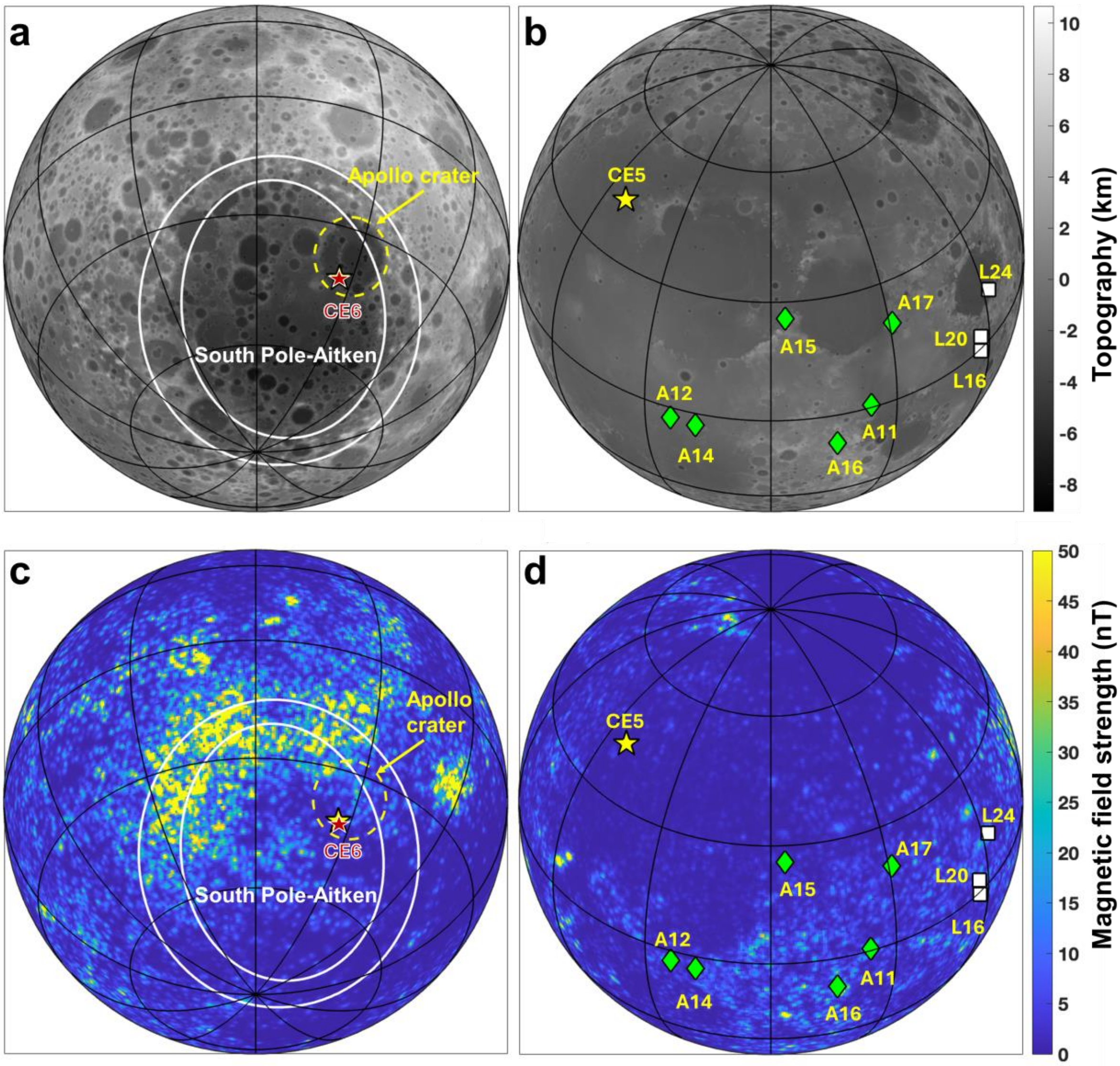

Supplementary Fig. 1 | Landing sites of lunar sample-return missions and their geological context. a, b, Topographic maps highlighting the landing site of the Chang'e-6 (CE6) sample-return mission on the lunar farside **(a)**, and landing sites of previous nearside lunar sample-return missions, including Appolo (A11, A12, A14, A15, A16, A17), Luna (L16, L20, L24), and Chang'e-5 (CE5) **(b)**. **c, d,** Maps illustrating crustal magnetic field strength distributions on the lunar farside **(c)** and nearside **(d)**, respectively (data from ref. 29). White ellipses oriented north-south **(a, c)** denote the best-fit boundaries of the South Pole-Aitken (SPA) Basin's inner floor and outer structural rim (adapted from ref. 23).

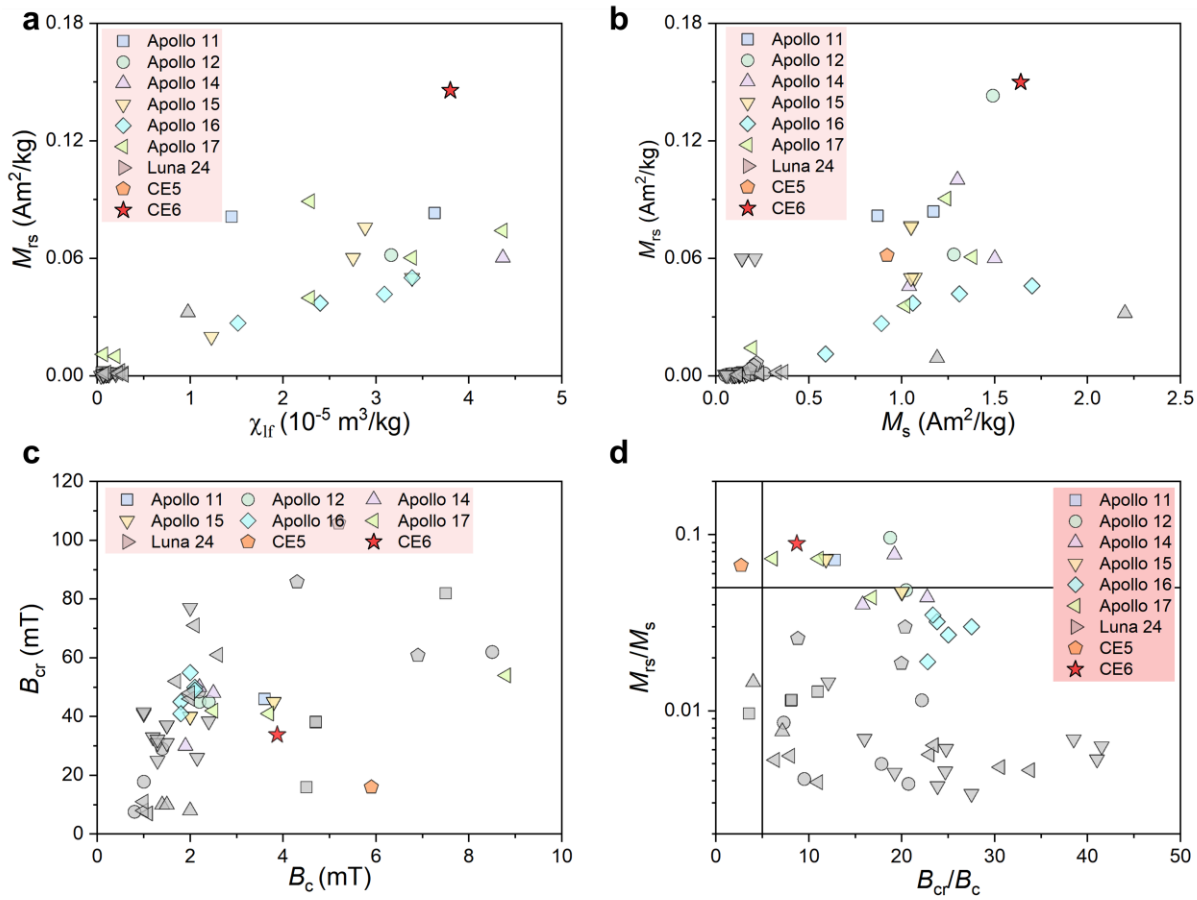

Supplementary Fig. 2 | Comparison of magnetic properties between CE6 soils and lunar soil and basaltic samples from previous missions. a, Low-frequency magnetic susceptibility (χ_{lf}) versus saturation remanence (M_{rs}). **b,** Saturation magnetization (M_s) versus M_{rs}. **c,** Coercivity (B_c) versus remanence coercivity (B_{cr}). **d,** Day plot showing remanence ratio (M_{rs}/M_s) versus coercivity ratio (B_{cr}/B_c). Colored symbols represent lunar soil samples (including CE6), whereas gray symbols indicate lunar basaltic rock samples. All data presented in this figure are sourced from Supplementary Data 1 and 2, where the corresponding references for each dataset are also clearly indicated.

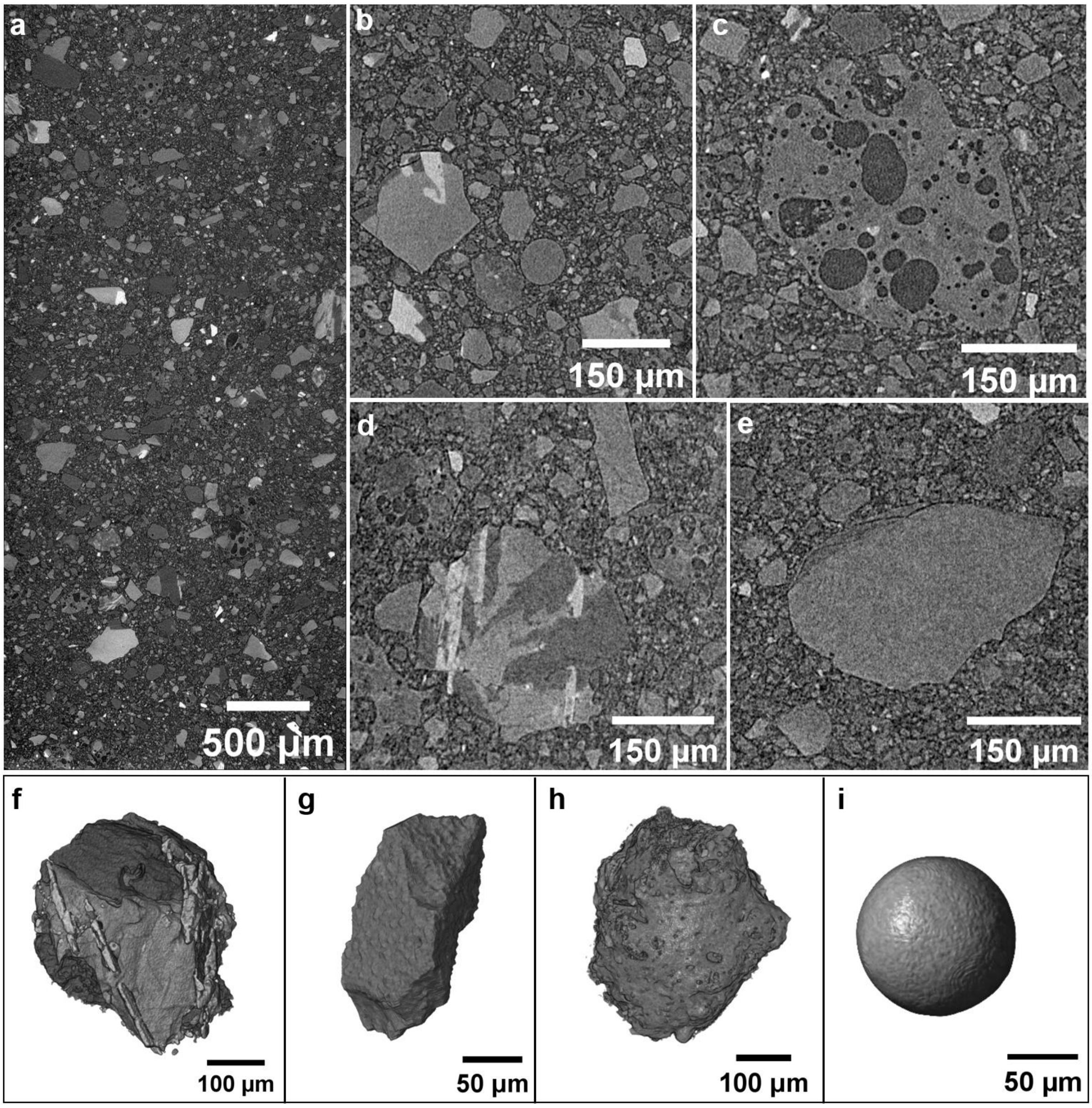

Supplementary Fig. 3 | Non-destructive 3D XRM imaging and reconstruction of CE6 soils. **a,** Virtual 2D slice obtained at ~1 μm voxel resolution, illustrating overall soil compostion. **b-e,** Magnified virtual 2D slices from representative microregions, achieved at ~500 nm vorxel resolution, highlighting detailed internal textures. **f-i,** 3D reconstructions of representative particles: basalt **(f)**, breccia **(g)**, aggregate **(h)**, and glass **(i)**, demonstrating compositional and morphological diversity.

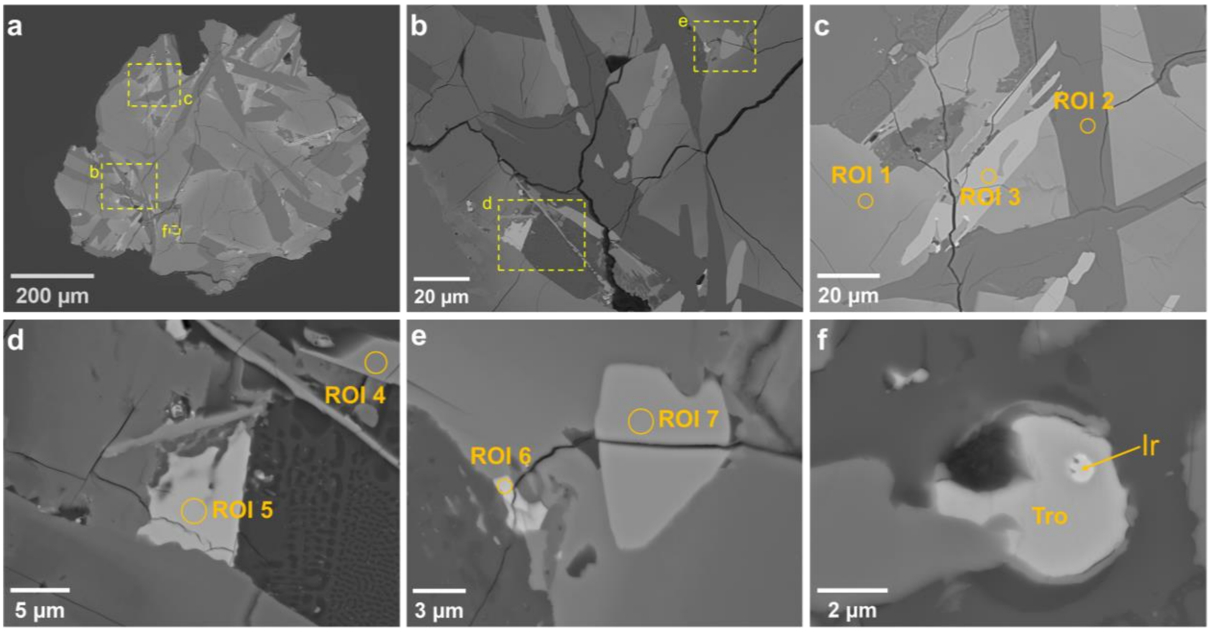

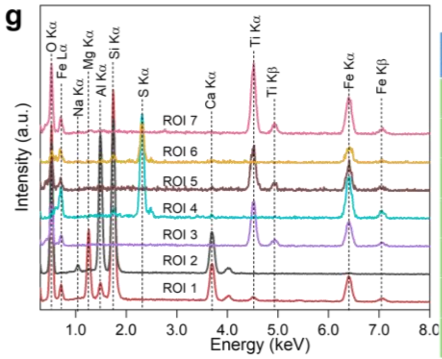

h

ROI	O (wt%)	Na (wt%)	Mg (wt%)	Al (wt%)	Si (wt%)	S (wt%)	Ca (wt%)	Ti (wt%)	Fe (wt%)	Mineral
1	38.9	—	8.0	1.6	22.9	—	8.5	1.3	18.9	Pyroxene
2	44.6	1.1	—	17.6	23.0	—	12.9	—	0.9	Plagioclase
3	29.8	—	—	—	—	—	—	30.7	39.6	Ilmenite
4	—	—	—	—	—	32.4	—	—	67.6	Troilite
5	26.7	—	—	—	—	—	—	29.8	43.5	Ilmenite
6	—	—	—	—	—	34.9	—	—	65.1	Troilite
7	30.4	—	—	—	—	—	—	30.6	39.0	Ilmenite

Supplementary Fig. 4 | BSE-SEM characterization of a representative basalt clast from CE6 soils. a, Overview BSE-SEM image of the basaltic grain exhibiting typical poikilitic textures. **b-f,** Magnified BSE-SEM images highlighting structural details of selected microregions within the basalt grain. **g,** SEM-EDXS spectra acquired from different regions of interests (ROIs), confirming compositional variations and identifying distinct mineral phases. **h,** Semi-quantitative elemental compositions dervied from SEM-EDXS spectra shown in panel **g**. Notably, detailed examination revealed only a single metallic iron (Ir) particle within this basalt section (panel f). Comprehensive SEM-EDXS elemental mapping corresponding to panel **f** is provided in Supplementary Fig. S5.

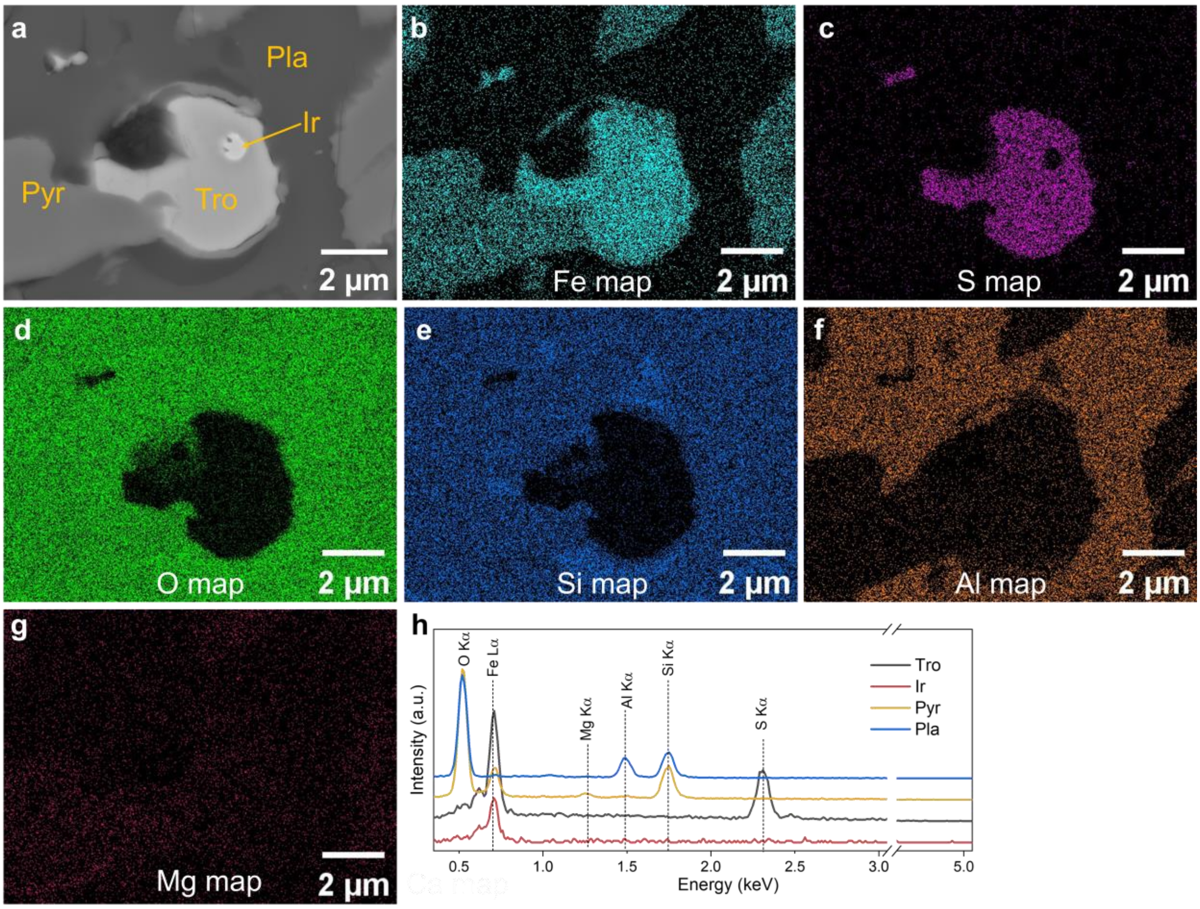

Supplementary Fig. 5 | SEM-EDXS characterization of a metallic iron particle in a CE6 basalt clast (analysis at 5 kV). a, BSE-SEM image showing a single meltallic iron (Ir) particle embedded within troilite (Tro). **b-g,** SEM-EDXS elemental maps of Fe (Fe Lα, **b**) S (S Kα, **c**), O (O Kα, **d**), Si (Si Kα, **e**), Al (Al Kα, **f**), and Mg (Mg Kα, **g**), illustrating clear compostional and spatial relationships among different mineral phases. **h,** SEM-EDXS spectra from selected mineral phases including trolite (Tro), metallic iron particle (Ir), pyroxene (Pyr), and plagioclase (Pla), confirming their distinct elemental signatures.

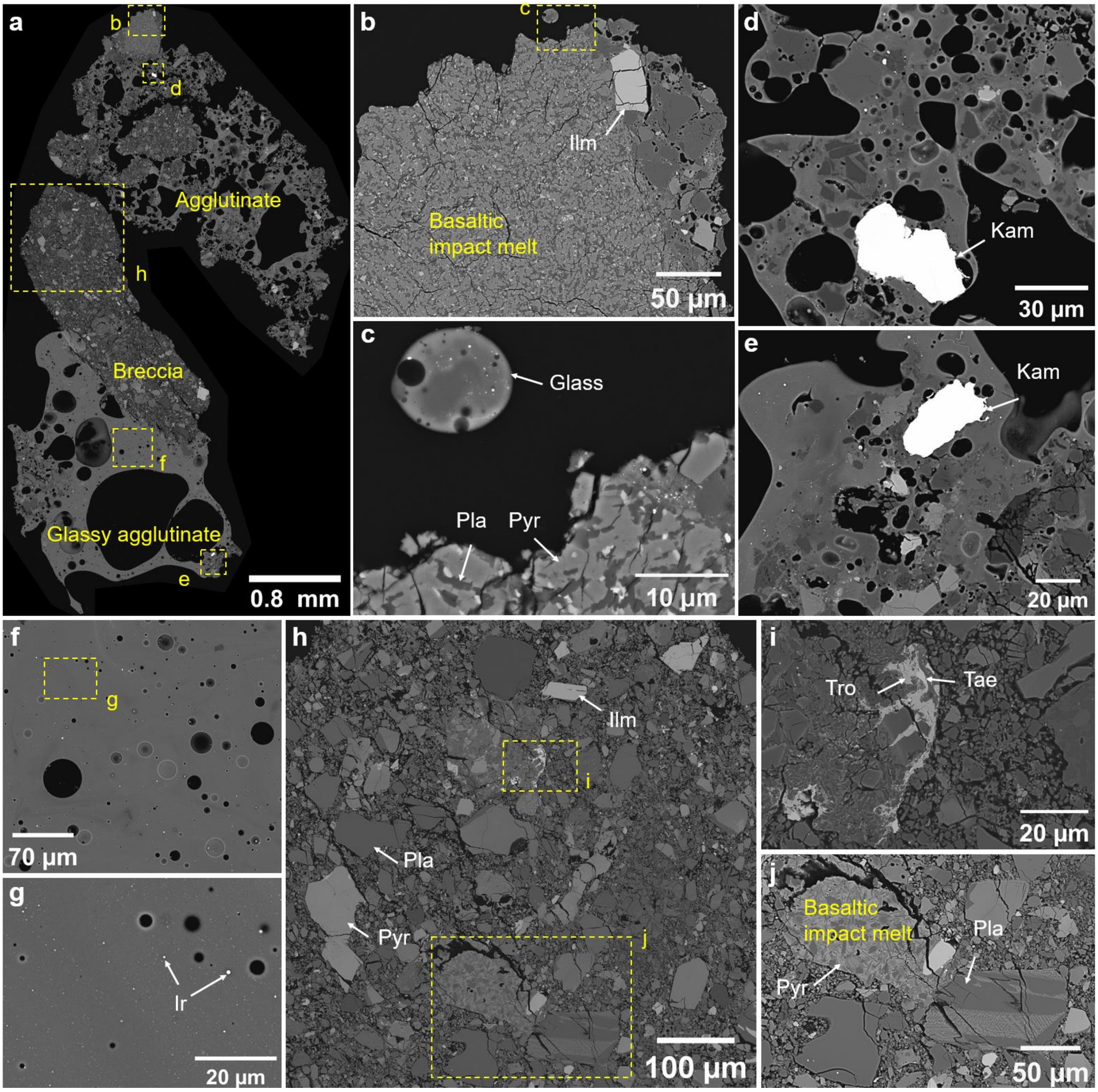

Supplementary Fig. 6 | BSE-SEM characterization of a representative non-basaltic clast from CE6 soils. a, Overview BSE-SEM image of a composite grain consisting of breccia, agglutinate, and glassy agglutinate. Areas outlined by dashed yellow boxes are magnified in panels **b-j**, highlighting distinct morphological and structural features. **b, c,** Basaltic impact melt **(b)** and glass clast **(c)** with characteristic internal textures. **d, e,** Structual details of agglutinate matrix containning embedded kamacite (Kam) microcystals. **f, g,** Glassy agglutinate regions containing abundant spherical metallic iron (Ir) particles with variable sizes. **h-j**, Structrual features within breccia, including microscale troilite (Tro) and taenite (Tae) veins **(i)** and basaltic impact melt textures **(j)**. Identified mineral phases include ilmenite (Ilm), plagioclase (Pla), pyroxene (Pyr),   troilite (Tro), kamacite (Kam), taenite (Tae), and metallic iron particles, confirmed by SEM-EDXS analysis (detailed compositional data provided in supplimentary Figs. S7-S13).

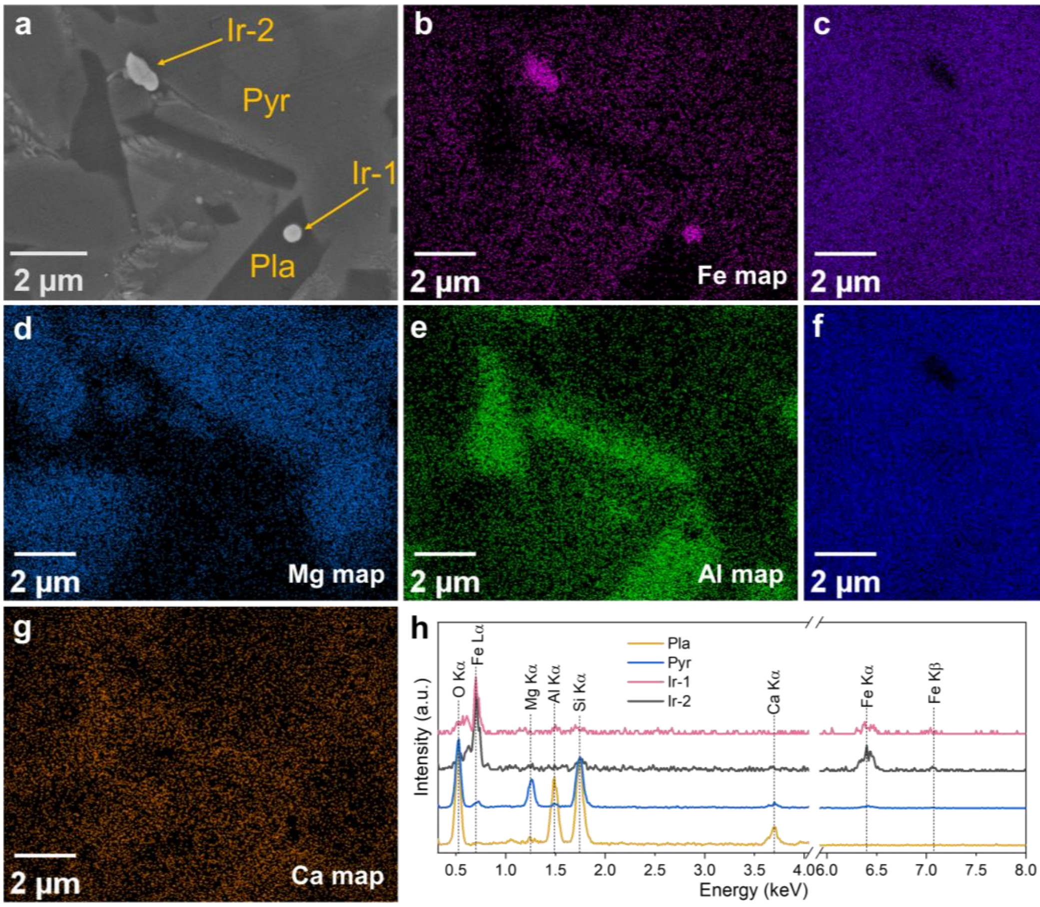

Supplementary Fig. 7 | SEM-EDXS characterization of metallic iron particles wthin CE6 basaltic impact melt (analysis at 15 kV). a, BSE-SEM image showing two distinct metallic iron particles (Ir-1, Ir-2), embedded within plagioclase (Pla, hosting Ir-1) and pyroxene (Pyr, hosting Ir-2). **b-g,** SEM-EDXS elemental maps illustrating spatial distributions and chemical relationships among mineral phases: Fe (Fe Kα, **b**), O (O Kα, **c**), Mg (Mg Kα, **d**), Al (Al Kα, **e**), Si (Si Kα, **f**), and Ca (Ca Kα, **g**). **h,** SEM-EDXS spectra from selected mineral phases, including metallic iron particles (Ir-1, Ir-2), pyroxene (Pyr), and plagioclase (Pla), confirming their distinct elemental signatures.

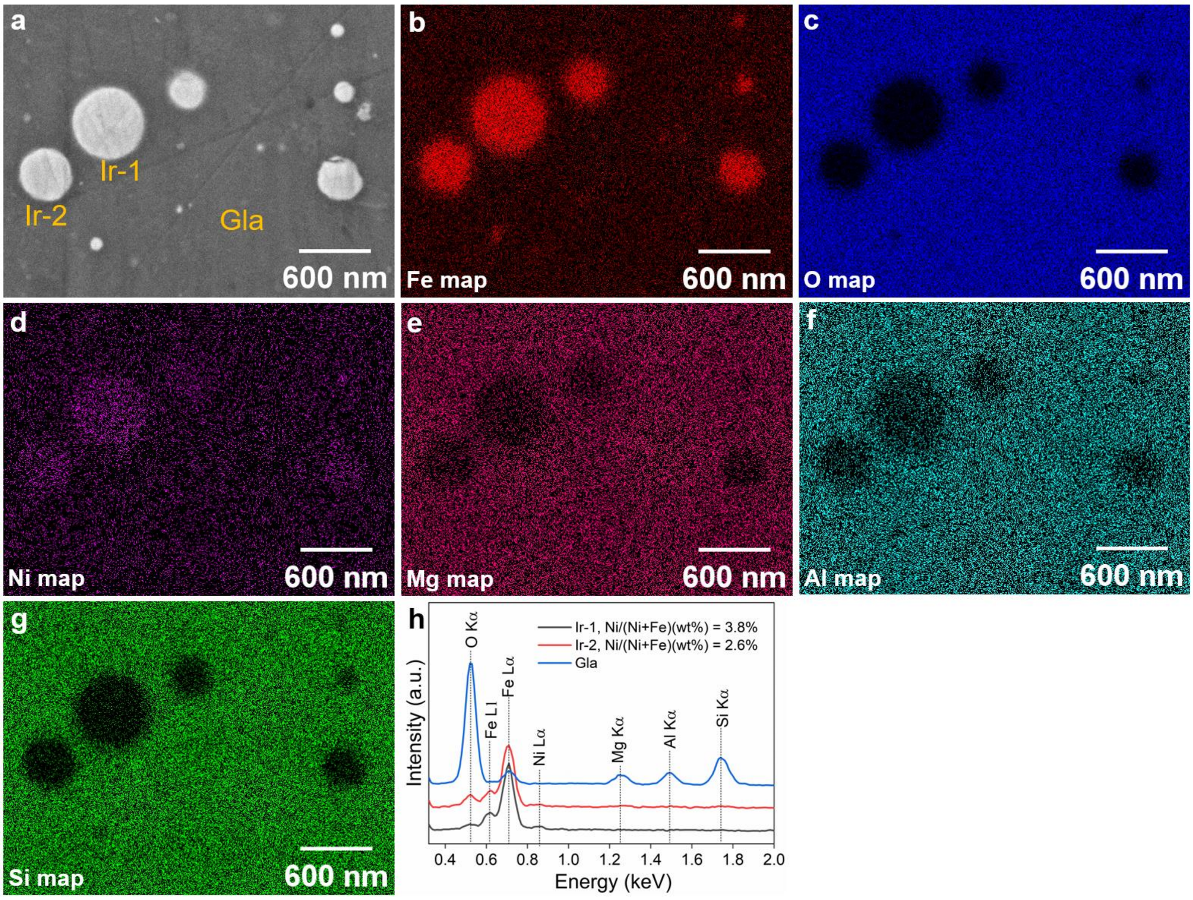

Supplementary Fig. 8 | SEM-EDXS characterization of metallic iron particles in a CE6 glassy aggregate (analysis at 5 kV). a, BSE-SEM image showing sperical meltallic iron particles of varying sizes embedded in a glassy matrix. **b-g,** SEM-EDXS elemental maps illustrating the distribution of Fe (Fe Lα, **b**), O (O Kα, **c**), Ni (Ni Lα, **d**), Mg (Mg Kα, **e**), Al (Al Kα, **f**), and Si (Si Kα, **g**), highlighting spatial and compositional relationships between metallic iron particles and the surrounding glassy matrix. **h,** SEM-EDXS spectra from selected metallic iron particles (Ir-1, Ir-2) and the glassy matrix (Gla), confirming clear elemental differences between phases.

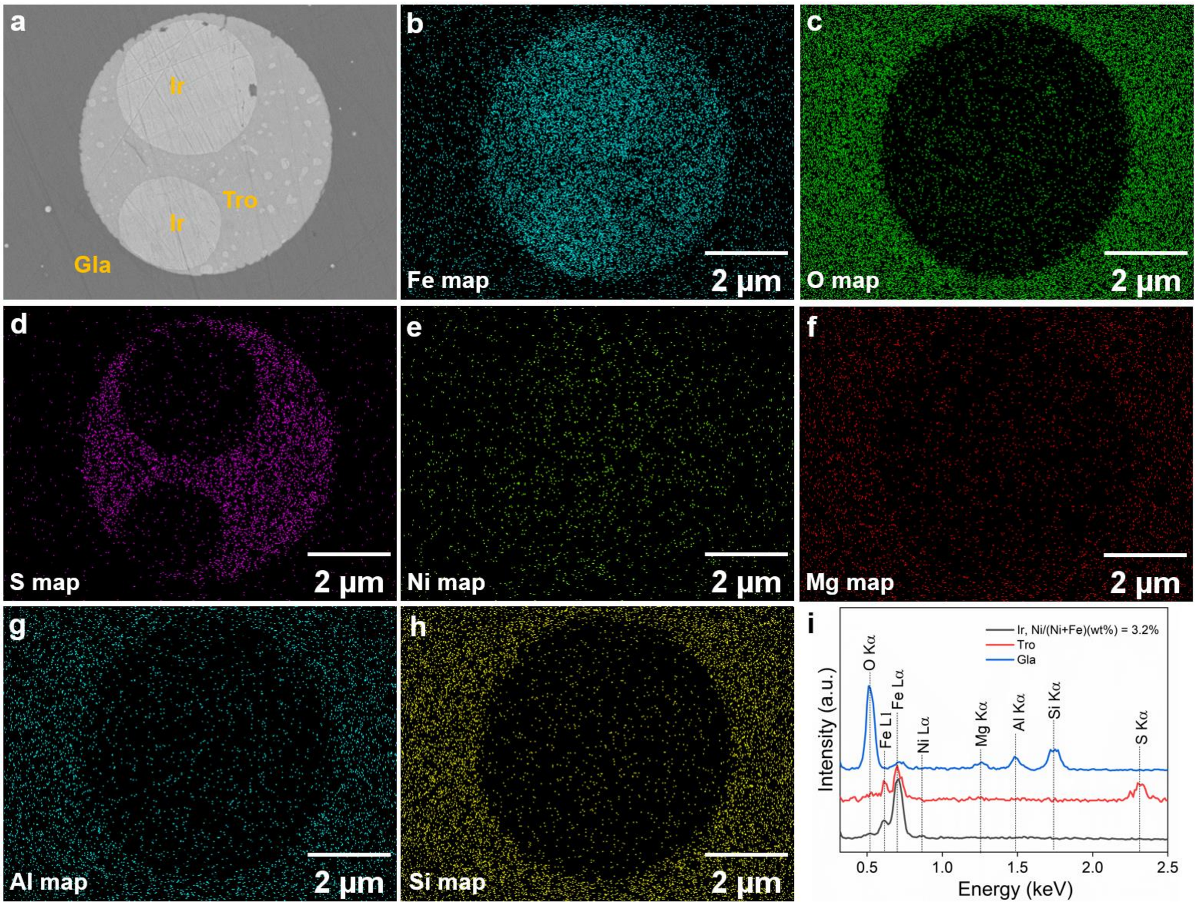

Supplementary Fig. 9 | SEM-EDXS characterization of a spherical trolite granule hosting two metallic iron particles (analysis at 5 kV). a, BSE-SEM image showing a spherical troilite (Tro) granule embedded in a glassy matrix (Gla), containing two large and several smaller metallic iron (Ir) particles. **b-h,** SEM-EDXS elemental maps illustrating the chemical distributions of Fe (Fe Lα, **b**), O (O Kα, **c**), S (S Kα, **d**), Ni (Ni Lα, **e**), Mg (Mg Kα, **f**), Al (Al Kα, **g**), and Si (Si Kα, **h**), highlighting spatial and compositional relationships among troilite, metallic iron particles, and the surrounding glassy matrix. **i,** SEM-EDXS spectra from selected microregions including metallic iron particle, troilite, and the glassy matrix, confirming their distinct elemental compositions.

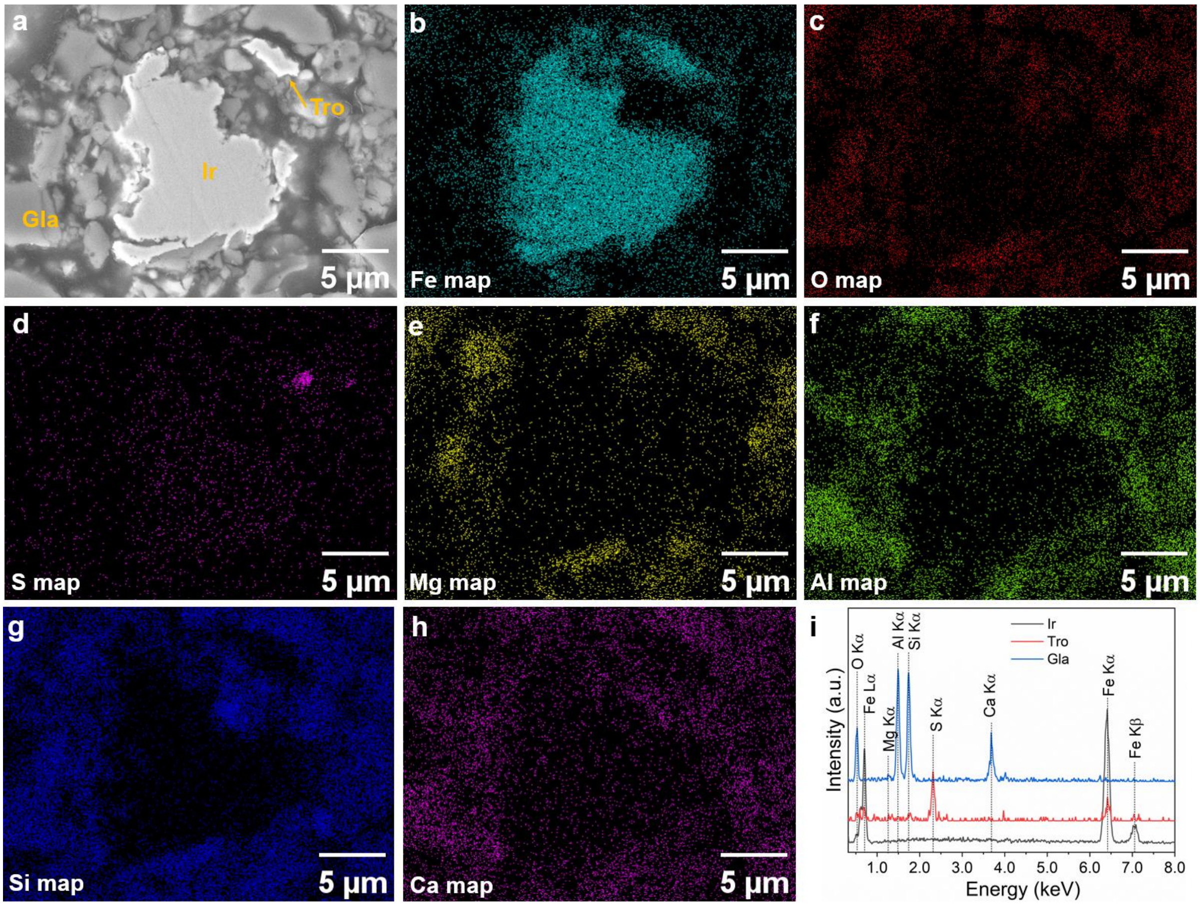

Supplementary Fig. 10 | SEM-EDXS characterization of a micron-scale irregualr iron particle within a glassy aggregate (analysis at 15 kV). a, BSE-SEM image showing a micron-scale irregualr iron (Ir) particle and an elonaged troilite (Tro) particle, both embedded within a glassy matrix (Gla). **b-h,** SEM-EDXS elemental maps illustrating distributions of Fe (Fe Kα, **b**), O (O Kα, **c**), S (S Kα, **d**), Mg (Mg Kα, **e**), Al (Al Kα, **f**), Si (Si Kα, **g**), and Ca (Ca Kα, **h**), highlighting spatial and compositional relationships between troilite, metallic iron particles, and the surrounding glassy matrix. **i,** SEM-EDXS spectra from metallic iron particle, troilite, and the glassy matrix, confirming distinct elemental compositions.

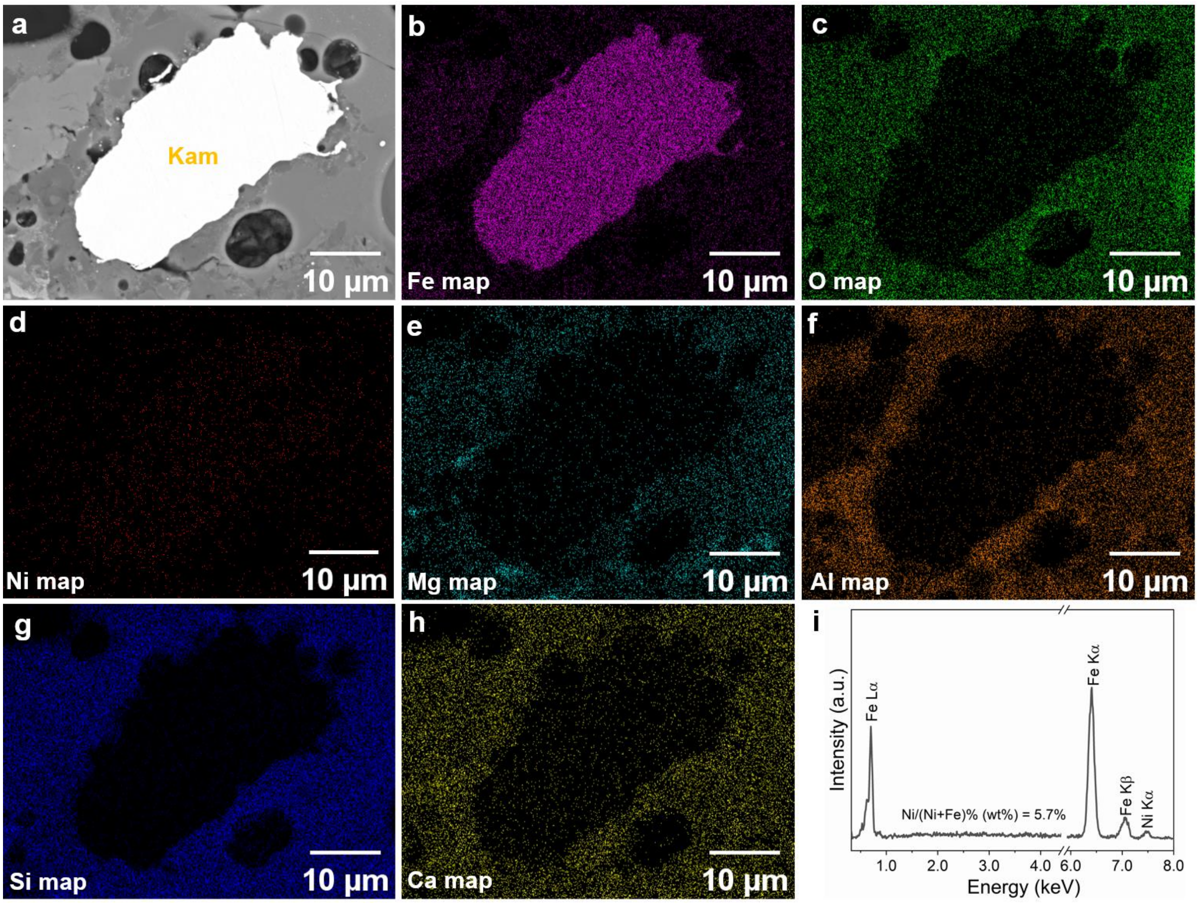

Supplementary Fig. 11 | SEM-EDXS characterization of a micron-scale elonaged Fe-Ni alloy (kamacite) particle within a glassy aggregate (analysis at 15 kV). a, BSE-SEM image showing kamacite (Kam) particle surrounded by glassy matrix. **b-h,** SEM-EDXS elemental maps illustrating distributions of Fe (Fe Kα, **b**), O (O Kα, **c**), Ni (Ni Kα, **d**), Mg (Mg Kα, **e**), Al (Al Kα, **f**), Si (Si Kα, **g**), and Ca (Ca Kα, **h**), highlighting chemcial compositioinal and spatial relationships between the kamacite and and surrounding glassy matrix. **i,** SEM-EDXS spectrum from the Fe-Ni particle, confirming its composition as kamacite.

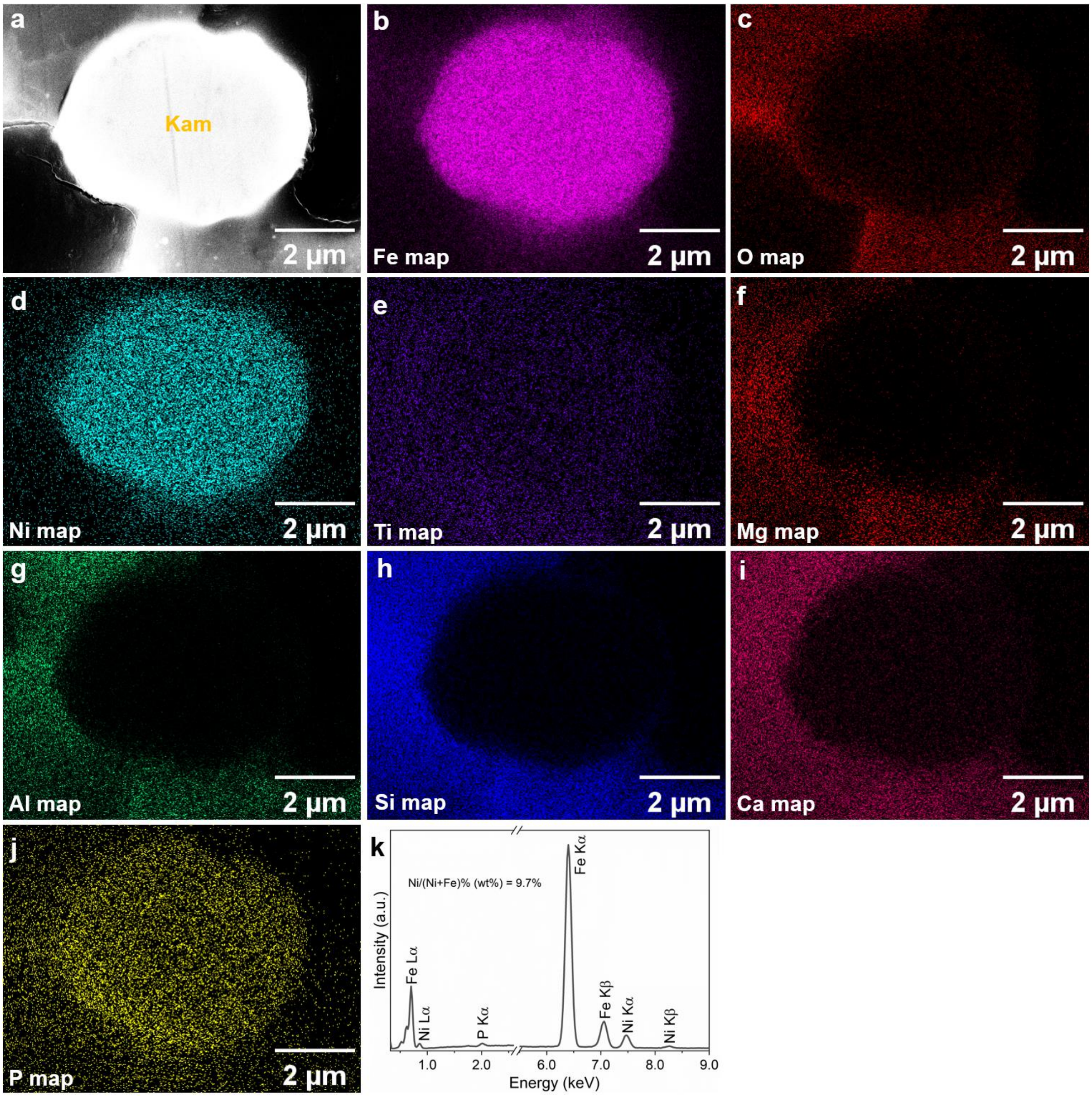

Supplementary Fig. 12 | SEM-EDXS characterization of an angular Fe-Ni alloy (kamacite) within a glassy aggregate (analysis at 15 kV). a, BSE-SEM image showing a micro-scale angular kamacite (Kam) particle surrounded by glassy aggregates. **b-j,** SEM-EDXS elemental maps illustrating distributions of Fe (Fe Kα, **b**), O (O Kα, **c**), Ni (Ni Kα, **d**), Ti (Ti Kα, **e**), Mg (Mg Kα, **f**), Al (Al Kα, **g**), Si (Si Kα, **h**), Ca (Ca Kα, **i**), and P (P Kα, **j**), highlighting chemical compositions and spatial relationships between kamacite and the surrounding glassy matrix. **k,** Rrepresentative SEM-EDXS spectrum acquired from the Fe-Ni alloy particle, confirming its composition as kamacite.

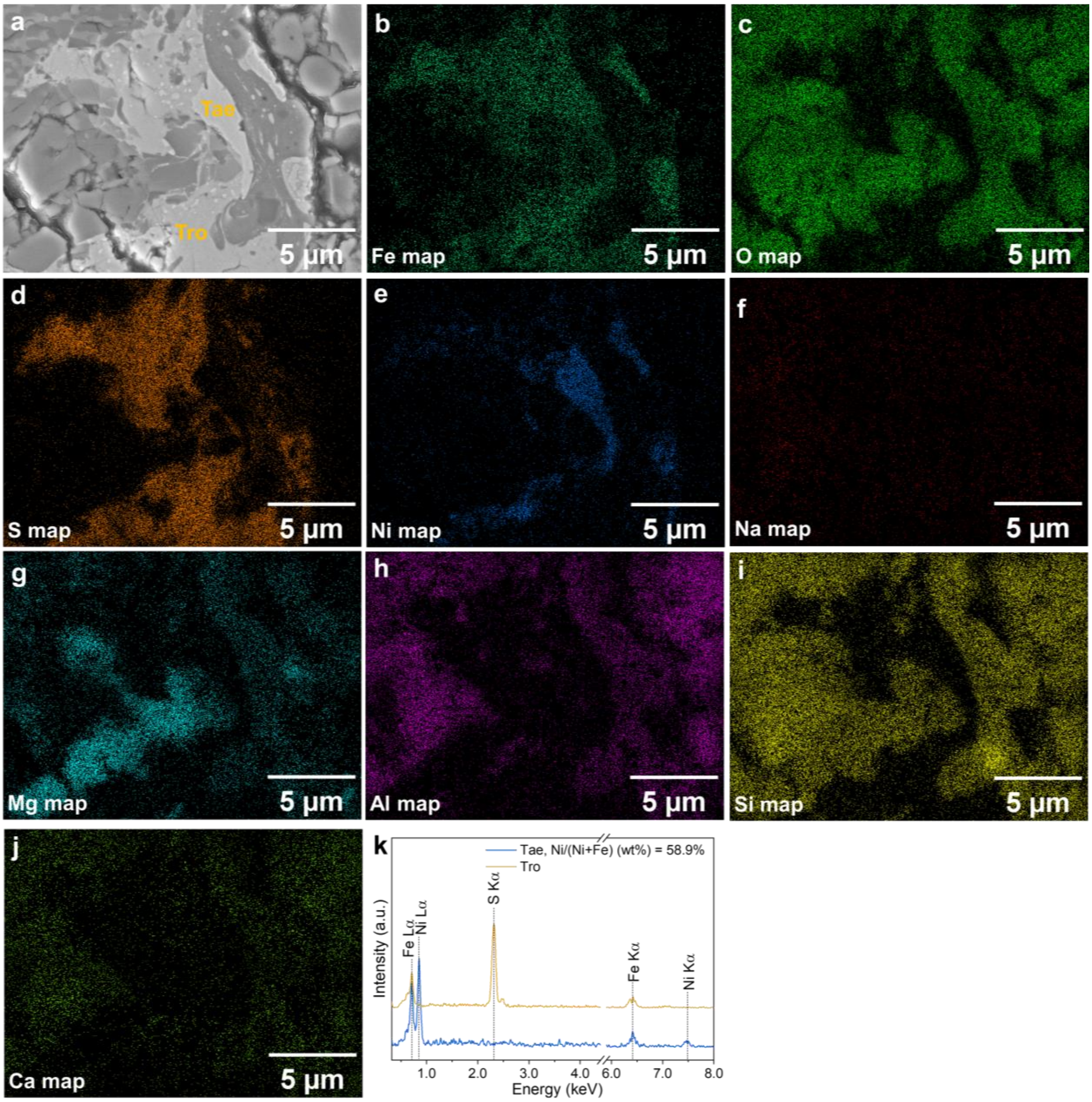

Supplementary Fig. 13 | SEM-EDXS characterization of troilite-taenite veins within a glassy aggregate (analysis at 15 kV). a, BSE-SEM image showing taenite (Tae) particles closely associated with, or embedded within, troilite (Tro) veins. **b-j,** SEM-EDXS elemental maps illustrating the distributions of Fe (Fe Kα, **b**), O (O Kα, **c**), S (S Kα, **d**), Ni (Ni Kα, **e**), Na (Na Kα, **f**) Mg (Mg Kα, **g**), Al (Al Kα, **h**), Si (Si Kα, **i**), and Ca (Ca Kα, **j**), highlighting compositional and spatial relationships among taenite, troilite, and the surrounding glassy matrix. **k,** Representative SEM-EDXS spectra collected from taenite and troilite, confirming the elemental composition of the Fe-Ni alloy as taenite.

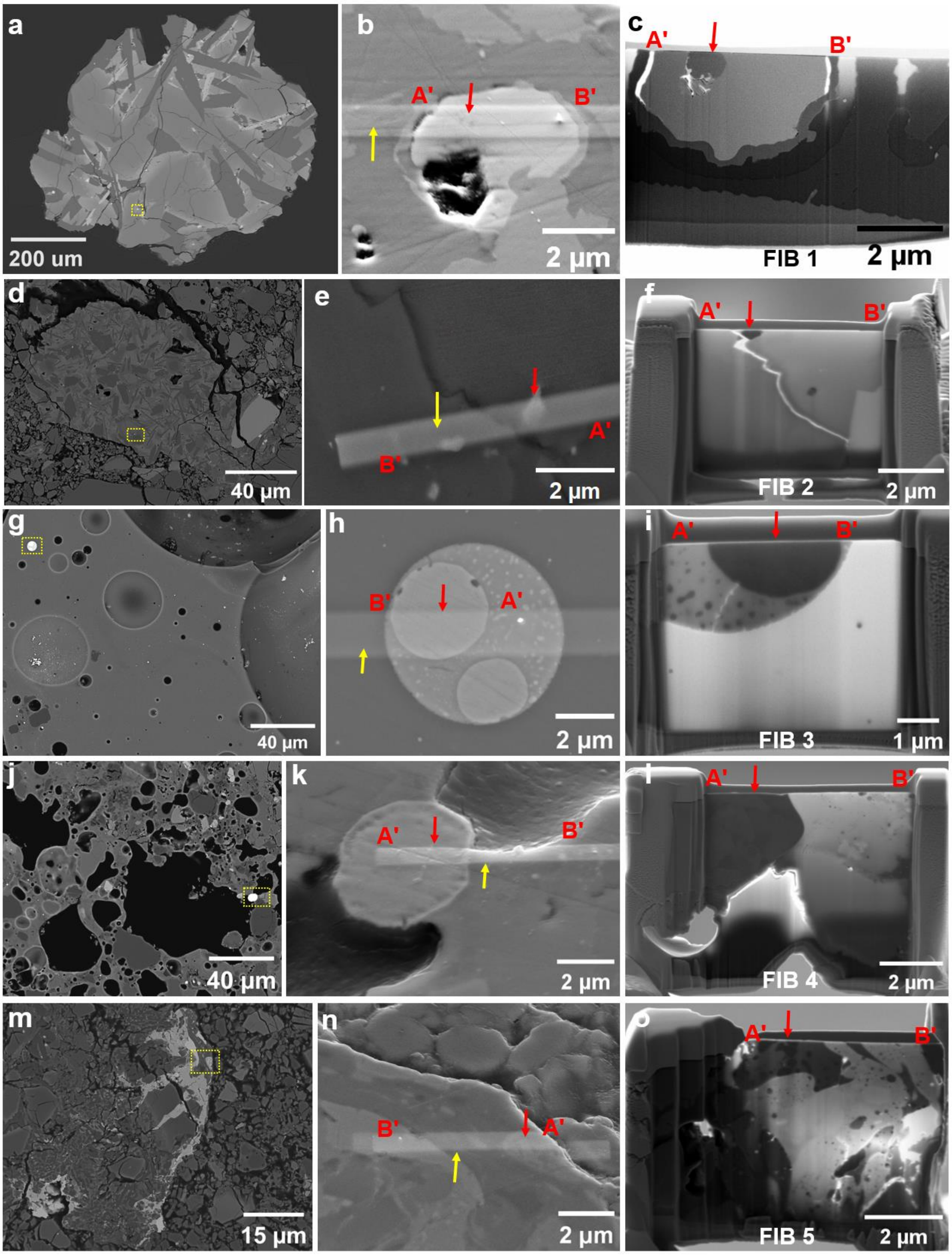

Supplementary Fig. 14 | Preparation of ultrathin FIB sections for TEM analyses from representative CE6 soil samples. BSE-SEM images (**a, d, g, j, m**) of selected CE6 soil samples (first column) showing diverse lithologies and mineral phases. Magnified images (**b, e, h, k, n,** corresponding to dashed yellow boxes in the first column) highlight microregions targeted for focused ion beam (FIB) milling. Yellow arrows mark the platinum coating appllied to protect the sample surface during milling and imaging. In the second and third columns, the labels A' and B', together with red arrows, denote the approximately corresponding positions before (second column) and after (thrid column) milling. The resulting ultrathin FIB sections (third column) represent basalt (**c,** FIB_1), basaltic impact melt (**f,** FIB_2), a spherical troilite granule containing metallic iron particles (**i,** FIB_3), a kamacite microcrystal (**l,** FIB_4), and a troilite-taenite vein (**o,** FIB_5).

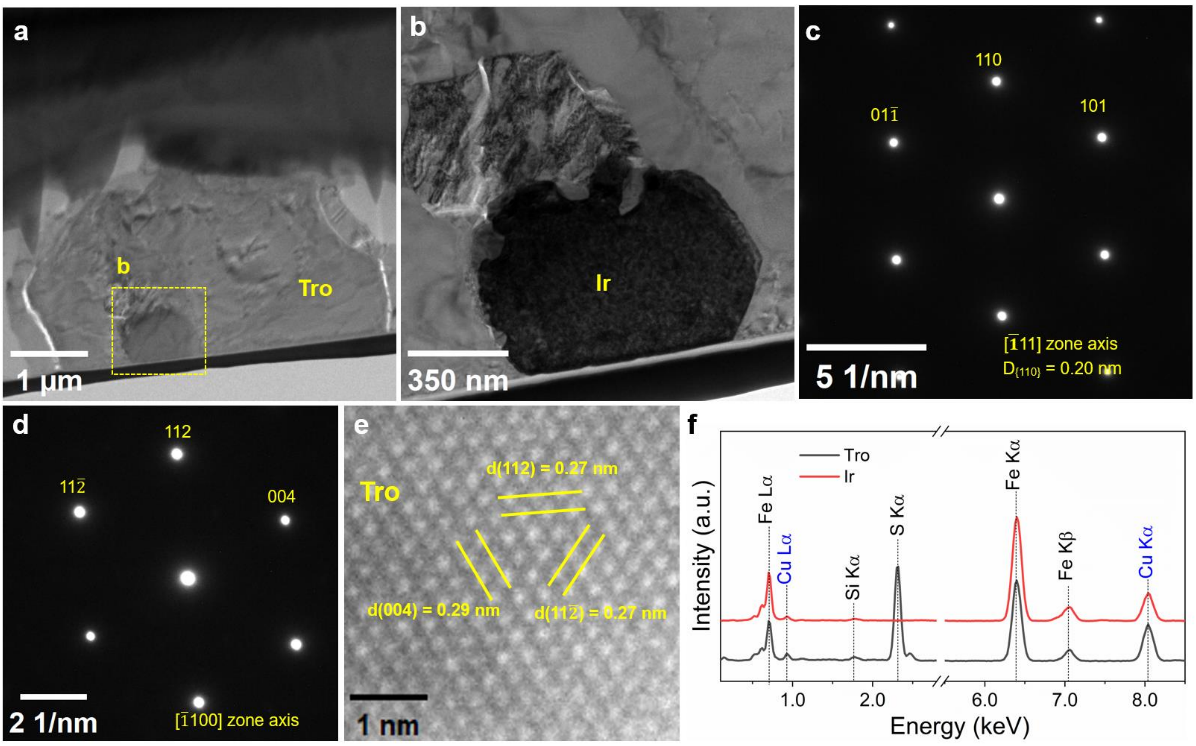

Supplementary Fig. 15 | TEM characterization of a metallic iron particle within the basalt sample FIB_1. a, Brigt-field transmission electron microscopy (TEM) image (partial view) showing the metallic iron (Ir) particle embedded within troilite (Tro). **b,** Magnified TEM image highlighting the euhedral morphology of the metallic iron particle. **c,** Selected-area electron diffraction (SAED) pattern of metallic iron particle viewed along the [$\bar{1}$11] crystallographic zone axis, with indexed diffraction spots and corresponding d-spacings. **d,** SAED pattern of troilite viewed from the [$\bar{1}$100] crystallographic zone axis, showing indexed Miller indices. **e,** High-resolution TEM (HRTEM) image of troilite with measured d-spacings. **f,** Representative TEM-EDXS spectra acquired from both troilite and metallic iron particle, confirming the absence of detectable Ni within the iron grain (Cu peaks originate from the TEM holder).

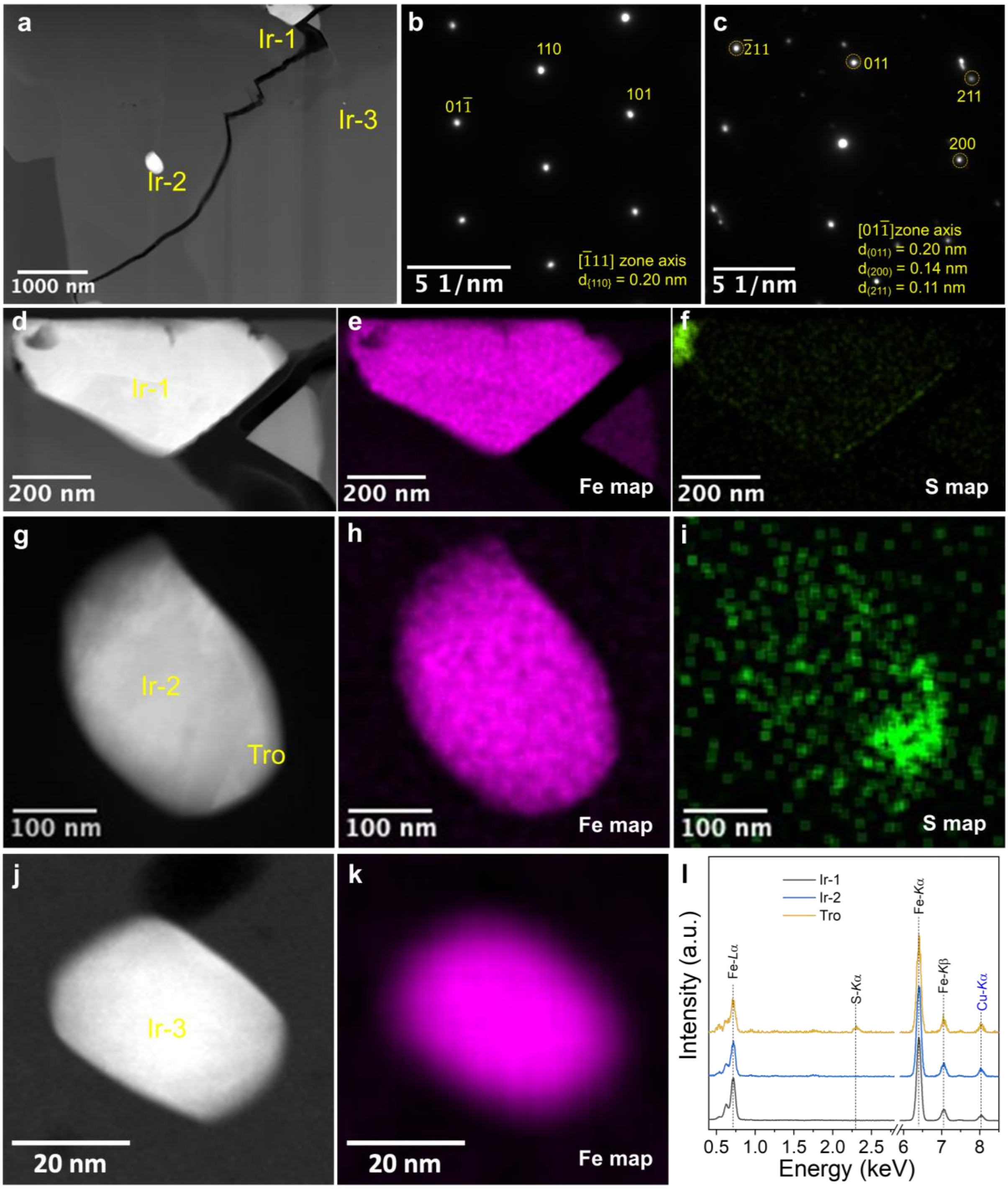

Supplementary Fig. 16 | TEM characterization of metallic iron particles in basaltic impact melt (sample FIB_2). a, High-angle annular dark-field scanning transmission electron microscopy (HAADF-STEM) image (partial view) showing three metallic iron particles (Ir-1, Ir-2, Ir-3) embedded within a glassy metrix. **b, c,** SAED patterns from particles Ir-1 (**b,** viewed along [$\bar{1}$11] axis) and Ir-2 (**c,** viewed along [01$\bar{1}$] axis), with indexed Miller indices and corresponding d-spacings. **d-f,** HAADF-STEM image **(d)** of particle Ir-1 and corresponding STEM-EDXS elemental maps of Fe (Fe Kα, **e**) and S (S Kα, **f**), revealing nanoscale troilite attached to the iron particle surface. **g-i,** HAADF-STEM image **(g)** of particle Ir-2 and corresponding STEM-EDXS elemental maps of Fe (Fe Kα, **h**) and S (S Kα, **i**), also showing surface-attached troilite. **j, k,** HAADF-STEM image **(j)** of particle Ir-3 and corresponding STEM-EDXS elemental map of Fe (Fe Kα, **k**). **l,** Representative STEM-EDXS spectra obained from partile Ir-1, Ir-2, and associated troilite (Tro), confirming no detectable Ni within the metallic iron grains.

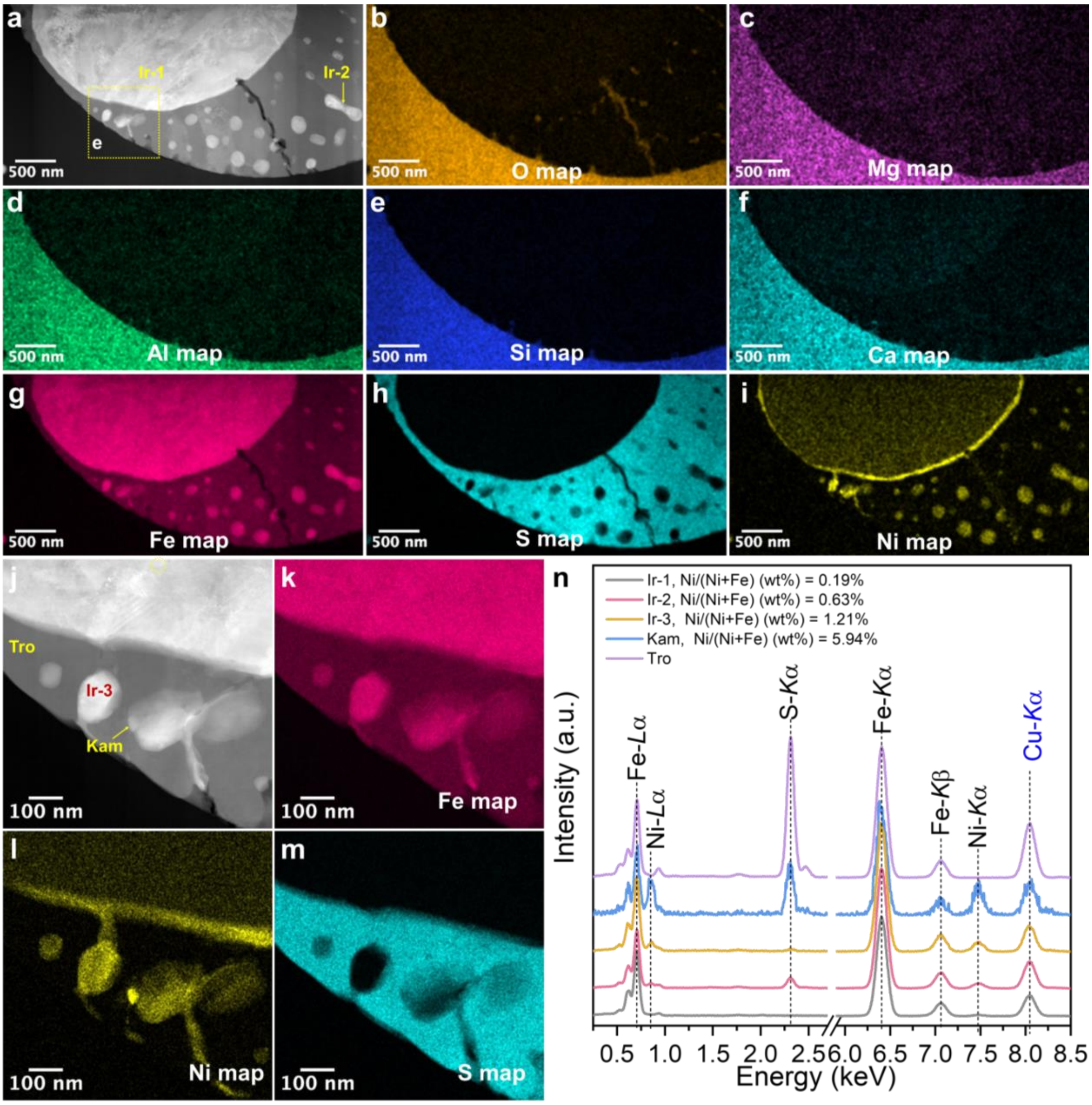

Supplementary Fig. 17 | TEM characterization of metallic iron particles in a sperical troilite granule embedded in a the glassy matrix (sample FIB_3). **a**, HAADF-STEM image (partial view) showing metallic iron particles with diverse sizes, morphologies, and nickel (Ni) contents embebdded within troilite (Tro), itself embeded in a glassy matrix. **b-i,** STEM-EDXS elemental maps of O (O Kα, **b**), Mg (Mg Kα, **c**), Al (Al Kα, **d**), Si (Si Kα, **e**), Ca (Ca Kα, **f**), Fe (Fe Kα, **g**), S (S Kα, **h**), and Ni (Ni Kα, **i**), illustrating compostional variations and spatial relationships among metallic iron particles, troilite, and the surrounding glassy matrix. **j-m,** Magnified HAADF-STEM image (outlined by a dahsed yellow box in panel **a**) of metallic iron particles and corresponding STEM-EDXS elemental maps of Fe (Fe Kα, **k**), Ni (Ni Kα, **l**), and S (S Kα, **m**), highlighting the heterogeneous Ni distributions. A small particle identified as kamacite (Kam) displays elevated Ni content. **n,** Representative STEM-EDXS spectra obtained from three metallic iron particles (Ir-1, Ir-2, Ir-3), kamacite (Kam), and troilite (Tro). Cu peaks originate from the TEM holder, and the minor S peak observed in the kamacite spectrum is attributed to signal overlap from adjacent troilite.

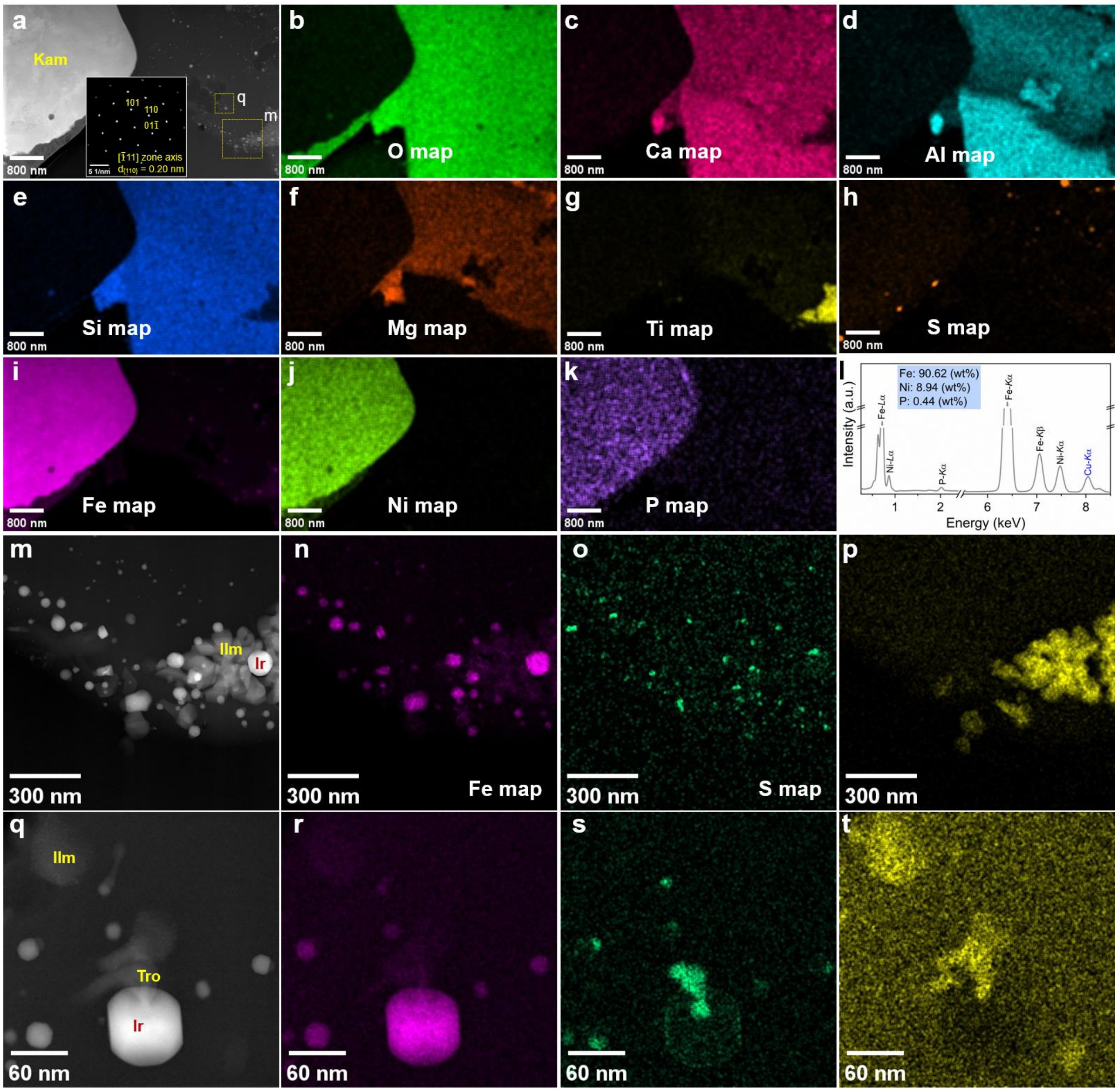

Supplementary Fig. 18 | TEM characterization of kamacite and metallic iron particles in a kamacite microcrystal and associated glassy matrix (sample FIB_4). a, HAADF-STEM image (partial view) showing a kamacite (Kam) particle (left) and surrounding glassy matrix with numerous embedded metallic iron particles. The inset presents a SAED pattern of kamactie viewed along the [$\bar{1}$11] crystographic zone axis, with indexed Miller indices and corresponding d-spacings. Kamacite has a body-centered cubic (BCC) atomic lattice structure, sharing similar d-sapcings with α-iron. Two microregions (outlined by dashed boxes) are magnified to detail the morphological and chemcial characteristics of metallic iron particles. **b-k,** STEM-EDXS elemental maps of O (O Kα, **b**), Ca (Ca Kα, **c**), Al (Al Kα, **d**), Si (Si Kα, **e**), Mg (Mg Kα, **f**), Ti (Ti Kα, **g**), S (S Kα, **h**), Fe (Fe Kα, **i**), Ni (Ni Kα, **j**), and P (P Kα, **k**), highlighting spatial relationships between kamacite and the surrounding glassy matrix. **l,** Representative STEM-EDXS spectrum obtained from the kamacite, confirming its composition with Ni/(Ni+Fe)% = 9.4 wt%. Note: STEM-EDXS analysis indicates that kamacite contains ~0.44 wt% P, and the Cu peak originates from the TEM holder. **M-t,** Magnified HAADF-STEM image of two selected microregions (**m, q,** outlined by dahsed yellow boxes in panel **a**) and their corresponding STEM-EDXS elemental maps of Fe (Fe Kα, **n, r**), S (S Kα, **o, s**), and Ti (Ti Kα, **p, t**). Results reveal nanoscale troilite (Tro) attachments on metallic iron particle edges, and submicron-scale ilmenite (Ilm) particles within the glassy matrix.

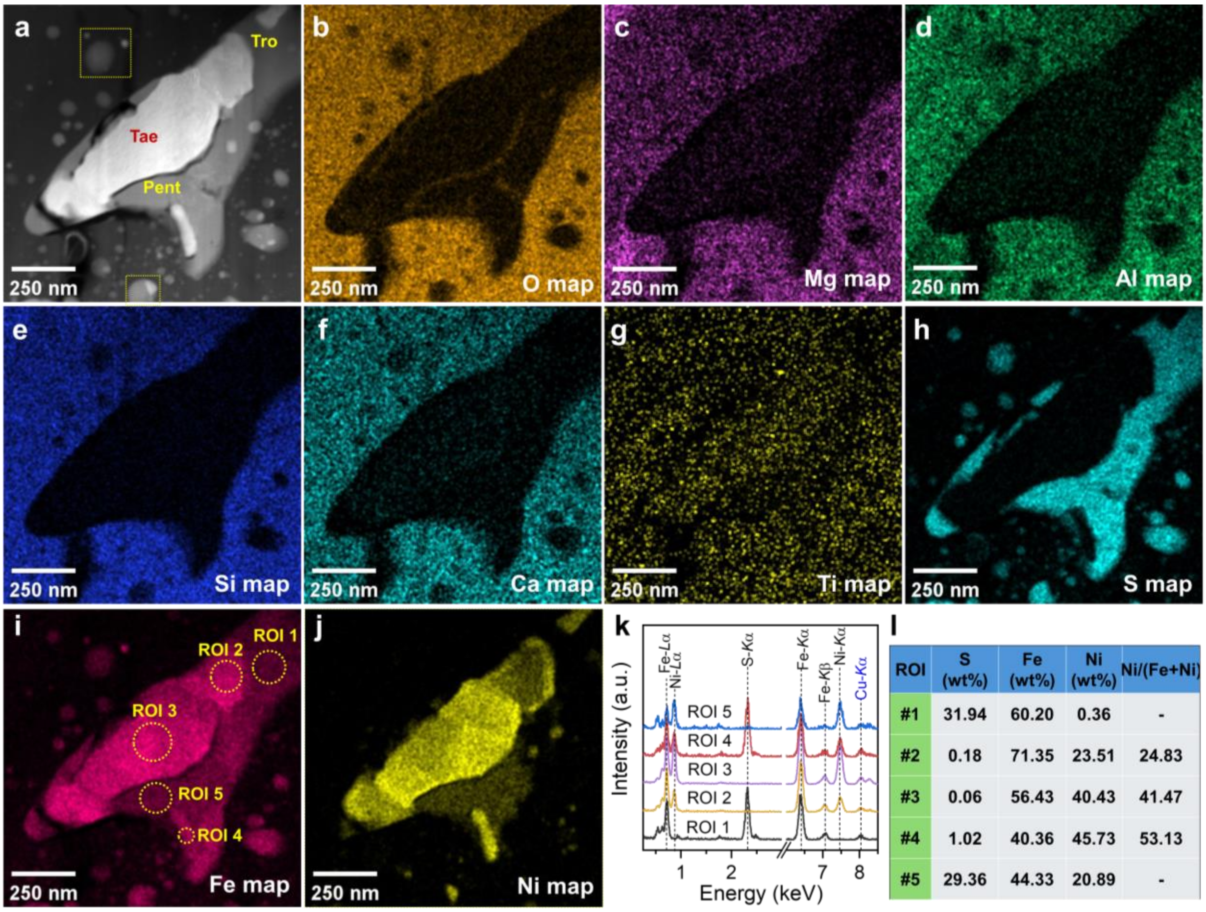

ROI	S (wt%)	Fe (wt%)	Ni (wt%)	Ni/(Fe+Ni)
#1	31.94	60.20	0.36	-
#2	0.18	71.35	23.51	24.83
#3	0.06	56.43	40.43	41.47
#4	1.02	40.36	45.73	53.13
#5	29.36	44.33	20.89	-

Supplementary Fig. 19 | TEM characterization of troilite-taenite-pentlandite assemblages within a troilite vein in breccia (sample FIB_5). a, HAADF-STEM image (partial view) showing troilite (Tro), taenite (Tae), and pentlandite (Pent) assemblages embedded within a glassy matrix. **b-j,** STEM-EDXS elemental maps of O (O Kα, **b**), Mg (Mg Kα, **c**), Al (Al Kα, **d**), Si (Si Kα, **e**), Ca (Ca Kα, **f**), Ti (Ti Kα, **g**), S (S Kα, **h**), Fe (Fe Kα, **i**), and Ni (Ni Kα, **j**), revealing compositional variations and spatial distributions of taenite, troilite, pentlandite, and the surrounding matrix. **k,** Representative STEM-EDXS spectra obtained from selected regions of interests (ROIs, outlined by dashed yellow circles in panel **i**), highlighting the heterogeneous distribution of Fe, Ni, and S whithin the assemblage. **l,** Semi-quantitative compositional results dervied from the STEM-EDXS spectra shown in panel **k**, confirming the identification of Fe-Ni alloys as taenite based on Ni concentrations.

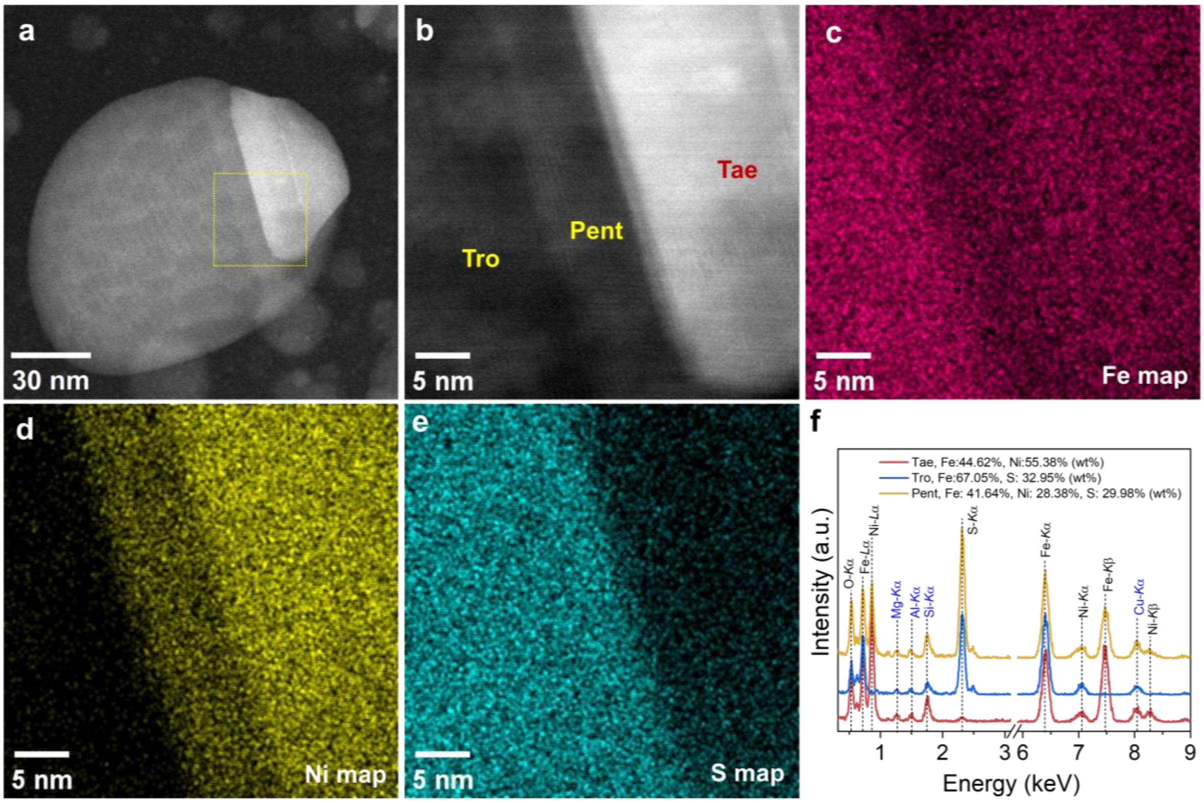

Supplementary Fig. 20 | TEM characterization of a troilite-pentlandite-taenite assemblage in sample FIB_5 (region outlined in Fig. S19a). a, HAADF-STEM image showing an ellipsed particle with distinct TEM contrast, composed of troilite (Tro, left), pentlandite (Pent, center), and taenite (Tae, right), embedded within a glassy matrix. **b,** Magnified HAADF-STEM image of the troilite-pentlandite-taenite interface (region outlined by dashed box in panel **a**). **c-e,** STEM-EDXS elemental maps of Fe (Fe Kα, **c**), Ni (Ni Kα, **d**), and S (S Kα, **e**), highlighting compositional heterogeneity and spatial relationships among the three phases. **f,** Representative STEM-EDXS spectra obtained from troilite, pentlandite, and taenite, confirming their compositions.

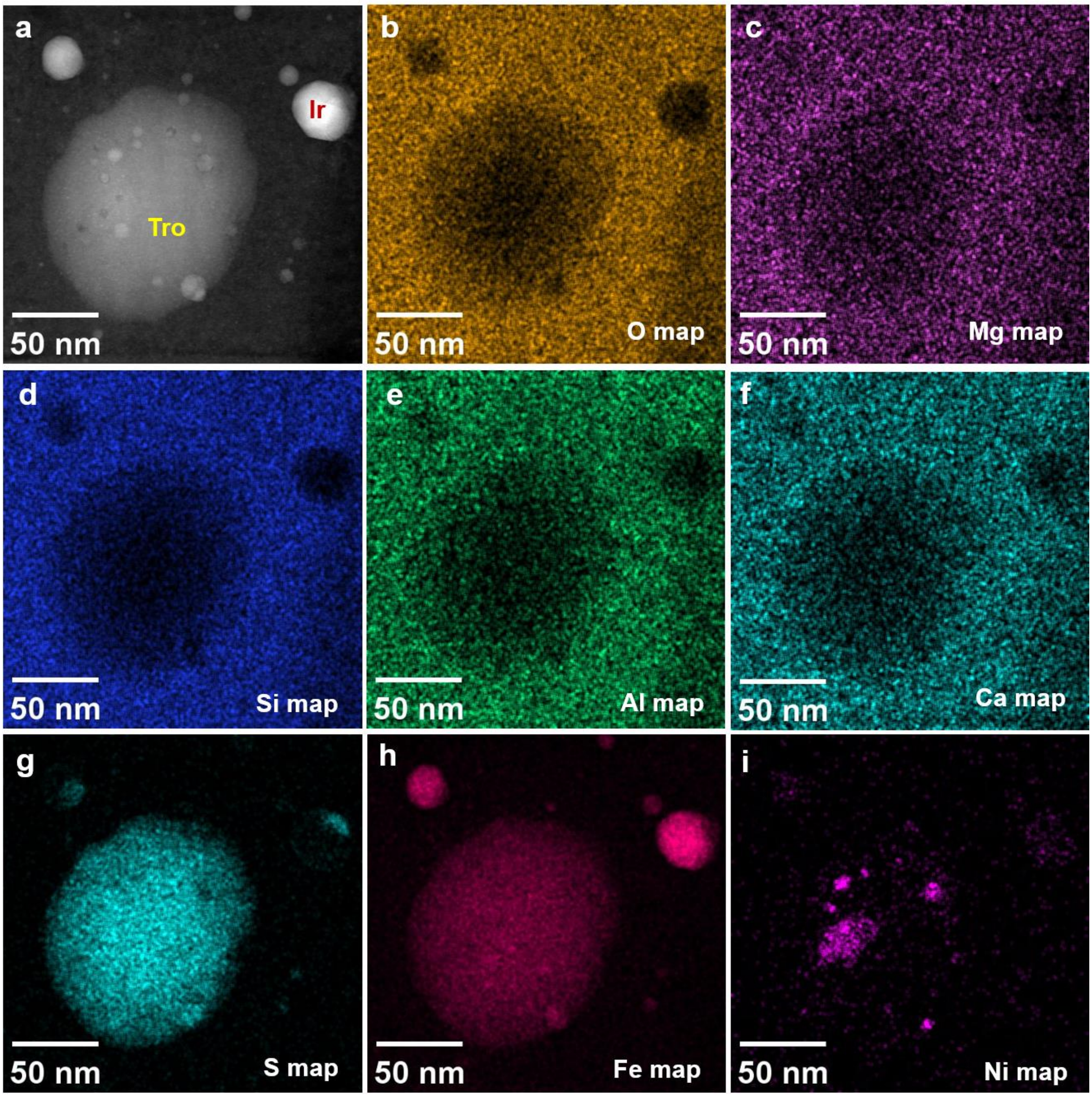

Supplementary Fig. 21 | TEM characterization of metallic iron and troilite particles in sample FIB_5 (region outlined in Fig. S19a, upper-left corner). a, HAADF-STEM image illustrating morphological and structural details of metallic iron (Ir) and troilite (Tro) particles embedded within a glassy matrix. **b-i,** Corrponsponding STEM-EDXS elemental maps of O (O Kα, **b**), Mg (Mg Kα, **c**), Si (Si Kα, **d**), Al (Al Kα, **e**), Ca (Ca Kα, **f**), S (S Kα, **g**), Fe (Fe Kα, **h**), and Ni (Ni Kα, **i**), highlighting the spatial relationships and compositional variations among troilite, metallic iron, and the surrounding matrix.